



## Full Text View

[Volume 32, Issue 1 \(January 2002\)](#)

### Journal of Physical Oceanography

Article: pp. 26–38 | [Abstract](#) | [PDF \(431K\)](#)

## Can Eddies Set Ocean Stratification?

**John Marshall, Helen Jones, Richard Karsten, and Richard Wardle**

*Department of Earth, Atmospheric, and Planetary Sciences, Massachusetts Institute of Technology, Cambridge, Massachusetts*

(Manuscript received July 21, 2000, in final form April 24, 2001)

DOI: 10.1175/1520-0485(2002)032<0026:CESOS>2.0.CO;2

### ABSTRACT

A simple theory is presented for the buoyancy anomaly and depth of penetration of a warm lens created by a surface buoyancy flux and Ekman pumping in an initially homogeneous, rotating fluid. It is assumed that the overturning of isopycnals induced by pumping and differential heating balances the counteroverturning tendency of baroclinic instability. Baroclinic eddies not only develop on the stratified lens, but also play a fundamental role in setting its stratification.

The theory is successfully tested against numerical and laboratory experiments in which the mechanically induced deepening of a buoyant lens is arrested by its baroclinic instability. Finally the possibility is discussed that the eddy transfer process studied here might play a role in setting the stratification and depth of the main thermocline in the ocean.

### 1. Introduction

In the earth's troposphere, radiative–convective imbalances lead to warming at low levels in the Tropics and cooling at upper levels in polar latitudes. Unless advective processes are invoked to carry energy upward and poleward, the pole–equator temperature gradient and the static stability of the troposphere would be several times that which is observed. But it is well known that the zonal wind in thermal wind balance with the meridional temperature gradient is baroclinically unstable. The ensuing large-scale eddies transfer energy poleward and upward, offsetting radiative imbalances and reducing the pole–equator temperature gradient toward observed values. Simple theories that invoke baroclinic eddy transfer—see for example [Stone \(1972\)](#)—offer plausible explanations for the zero-order physics and dynamics at play.

#### Table of Contents:

- [Introduction](#)
- [Equilibration of a warm-water](#)
- [Theoretical interpretation](#)
- [Conclusions](#)
- [REFERENCES](#)
- [TABLES](#)
- [FIGURES](#)

#### Options:

- [Create Reference](#)
- [Email this Article](#)
- [Add to MyArchive](#)
- [Search AMS Glossary](#)

#### Search CrossRef for:

- [Articles Citing This Article](#)

#### Search Google Scholar for:

- [John Marshall](#)
- [Helen Jones](#)
- [Richard Karsten](#)
- [Richard Wardle](#)

Consider, now, a subtropical ocean differentially warmed at the surface under the influence of anticyclonic wind stress

curl forcing. Ekman layers pump the warm fluid down into the interior, inducing increasingly large lateral temperature gradients while deepening the vertical stratification. Drawing an analogy with the earth's troposphere, one might suppose that baroclinic eddies develop to carry the warm fluid away laterally, to sites where excess warmth can be lost to the atmosphere, as represented schematically in [Fig. 1](#). In so doing, the tendency to increase the tilt of the isotherms—here a consequence of mechanical pumping and differential heating—is balanced by the counteroverturning tendency consequent on baroclinic instability. If one hypothesized a balance between these tendencies, then one could determine the temperature and depth of the warm lens at which its creation and deepening by air–sea interaction was arrested by baroclinic instability. Exploring the ramifications of this idea in a controlled setting is the goal of the present study. The notion is alluded to in [Gill et al. \(1974\)](#), where it is hypothesized that the rate of increase in potential energy of the main thermocline due to the wind acting on its preexisting stratification, is balanced by its rate of reduction in baroclinic instability.

The foregoing is our geophysical motivation, but here we explore the fundamental idea by studying a laboratory and numerical analogue. The experiment is abstracted so far away from the oceanographic context that its relevance is readily questioned. However, the laboratory experiment is of interest in its own right because it conjoins in a simple way the mechanical and buoyancy forcing of a rotating fluid. In [section 2](#), we set up a highly idealized thought experiment and realize it in both laboratory and complementary numerical experiments. Fluid warmed beneath a rotating disc is pumped down by the mechanical action of that disc into the ambient, initially isothermal, rotating fluid beneath. A warm lens develops that deepens by pumping until it becomes baroclinically unstable. The baroclinic eddies arrest the deepening of the lens, sweeping the warm water away laterally, thereby controlling its temperature and depth. In [section 3](#) we develop a theoretical model that yields predictions for the buoyancy anomaly and depth of the lens. We then test those predictions using our numerical and laboratory experiments. We conclude in [section 4](#) and discuss the possible geophysical ramifications of our study for the ocean in the context of previous studies concerning ocean stratification. Tantalizingly, for oceanographic parameters, our formulas yield plausible numbers for the great subtropical gyres of the ocean. However, because of its simplicity—geometry, the absence of a  $\beta$  effect, no western boundary currents, etc.—the oceanographic relevance of the warm, pumped lens studied here is unclear. In a companion paper, therefore, we set up a physical analogue that can be much more readily associated with the ocean and apply the ideas presented here more directly to the Antarctic Circumpolar Current—see [Karsten et al. \(2001\)](#).

## 2. Equilibration of a warm-water lens

### a. Laboratory realizations

#### 1) SET UP OF LABORATORY EXPERIMENT


We designed a laboratory experiment in which a rotating tank of water of initially uniform temperature is warmed at its surface under a rotating disc. The apparatus is shown schematically in [Fig. 2](#). The cylindrical tank, of diameter 1.15 m and depth  $H = 15$  cm, intended to provide an ample reservoir of unstratified water within which a heated lens could develop freely, was rotated in an counterclockwise sense at a rate  $f_{\text{tank}}$ , typically once every 15 seconds. Pumping and warming were controlled by positioning a heated, rotating “Plexiglass” disc on the surface of the fluid, which had a radius  $\sim 55$  cm, slightly less than that of the tank. The rate at which the disc rotated,  $f_{\text{disc}}$ , was controlled via a coaxial shaft by a motor mounted above the turntable. Glued to the underside of the disc, and insulated from it, was a circular heating pad of considerably smaller radius,  $\sim 15$  cm, inset so that the Plexiglass disk and heating pad presented a flat surface to the underlying fluid.

The thermal forcing provided by the heating pad was controlled by setting and monitoring current and voltage to ensure an uninterrupted and constant heating rate for the duration of the experiment. The heating pad could provide power between 0 and 3000 W, and so warm a 5-cm layer of fluid by a few degrees in 10 minutes or so.


Mechanical forcing was provided by the rotation of the large Plexiglass disc itself. According to Ekman theory, a disc in solid-body rotation, applying a torque to an underlying homogeneous rotating fluid, induces a spatially constant vertical velocity beneath it ([Hide and Titman 1967](#)) of strength


$$w_E = \frac{\Delta f}{2} \left( \frac{\nu}{2f_{\text{tank}} + \Delta f} \right)^{1/2}, \quad (1)$$

where  $f_{\text{tank}} = 2\Omega_{\text{tank}}$  with the tank rotation rate in  $\text{rad s}^{-1}$ ,  $\Delta f = f_{\text{disc}} - f_{\text{tank}}$  is the rotation rate of the disc relative to the tank,  $f_{\text{disc}}$  is the disc rotation rate, and  $\nu$  is the molecular viscosity of water (see, e.g., [Pedlosky 1987](#)). To induce pumping ( $w_E < 0$ ),  $f_{\text{disc}} < f_{\text{tank}}$ , that is the disc must be rotated in the same sense as the underlying tank (counterclockwise) but at a

slower rate. For the differential rotation rates typical of our experiments (see [Table 1](#) ) , and noting that  $\nu = 10^{-6} \text{ m}^2 \text{ s}^{-1}$ , typical Ekman vertical velocities of  $\sim -1/10 \text{ mm s}^{-1}$  are induced. Thus water beneath the disc could be pumped to a depth of some 6 cm in 10 minutes, or typically 40 rotation periods. This combination of a large disc providing mechanical torque and a smaller embedded heating disc achieved our objective of applying controlled levels of Ekman pumping and differential heating to the underlying fluid. Use of the larger “mechanical” disc, cut to roughly fit the circular tank itself, was found to effectively suppress edge effects, which might otherwise have compromised the baroclinic instability of the developing thermal lens.


Under the action of the warmed disc we observe, after 10 minutes or so, a lens of fluid forming which is a few degrees warmer than its surroundings, reaching down to a depth of a few centimeters. The deformation radius of such a lens is, as we shall see, only a few centimeters, considerably smaller than the lens radius. Thus the lens is susceptible to baroclinic instability and, once unstable, continually breaks up in to eddies. A typical experiment lasted for around one hour, with the evolving lens and its instabilities exhibiting timescales from minutes to tens of minutes. The vertical temperature profile at the center of the tank was recorded every 5 seconds by a vertical thermocouple array, fast enough to resolve all motions without aliasing. The flow was visualized by injecting a neutrally buoyant red dye in to the fluid on the periphery of the heating pad and recording its evolution on video and photograph.


In all, ten laboratory experiments were carried out for rotation periods ( $4\pi/f_{\text{tank}}$ ) ranging between 5 and 25 seconds, heating of between  $100$  and  $3000 \text{ W m}^{-2}$ , and pumping between 10 and 70 centimeters per hour. Specific parameter combinations are set out in [Table 1](#) . The surface buoyancy flux,  $B_o$ , is calculated directly from the power provided to the heating pad according to the relation  $B_o = g\alpha q/\rho c_p$  where  $g$  is the acceleration due to gravity,  $\alpha$  the thermal expansion coefficient of water,  $q$  the heat flux in  $\text{W m}^{-2}$ ,  $\rho$  is density and  $c_p$  the specific heat capacity. Given the molecular viscosity of water  $\nu = 10^{-6} \text{ m}^2 \text{ s}^{-1}$ , the pumping rate is calculated on the basis of  $f_{\text{tank}}$  (the tank rotation rate) and  $\Delta f$  (the differential rotation rate of the surface disc) according to [\(1\)](#).

We now go on to describe the evolution of our reference laboratory lens (associated parameters are highlighted in bold in [Table 1](#) ).


## 2) OBSERVED EVOLUTION OF THE LENS

The earliest growth of the lens appears to be laminar and symmetrically disposed about the axis of rotation. However, as it deepens, it becomes hydrodynamically unstable and spawns baroclinic eddies. The lens becomes increasingly distorted and the rate of deepening visibly slows until it is finally arrested by its own instability. Initially the instability is of high mode number, but as the eddies grow to finite amplitude they appear to coalesce producing waves of much larger amplitude and wavelength than the initial instability.

[Figure 3](#)  shows a snapshot of the tank once equilibrium has been achieved. Baroclinic eddies can be clearly seen sweeping fluid outward from the heating disc. This evolution was typical of all our experiments: Deepening of the lens was in all cases arrested by baroclinic instability, with varying degrees of finite amplitude eddy coalescence.

In the absence of a balancing heat sink, the average temperature of the tank will continually rise with time at a very slow rate determined by the heating. We define the temperature anomaly as the variation from this average value. Hereafter, the temperature will be in reference to this temperature anomaly. [Figure 4](#)  shows the evolution of the temperature anomaly beneath the disc in the reference experiment, measured by the vertical thermocouple array at the center of the disc. For the first 10 minutes—40 rotations or so—the temperature beneath the disc increases steadily. But once baroclinic eddies begin to exchange fluid, the temperature increase slows, finally fluctuating around a steady value. Thus a stratification has been created beneath the lens, the magnitude of which is set by the collusion of mechanical/buoyancy forcing and baroclinic instability.

## 3) MEASUREMENT OF DEPTH AND TEMPERATURE OF EQUILIBRATED LENS

Two quantities characterize the lens—its temperature and depth. [Figure 5](#)  shows the mean temperature profile obtained by averaging the temperature over a one hour period of the steady state established once lens equilibration had been reached. We see, and consideration of self-similarity in the heat flux balances suggest, that the vertical profile is of exponential form. By fitting an exponential curve to the temperature profile, we obtain an  $e$ -folding depth and maximum surface temperature of the lens.


In order to develop a complete theory for the dynamics of an equilibrated lens requires a sense of the time mean structure *off-axis*, which was not directly measured in the laboratory. To analyze the three-dimensional temperature distribution and

accompanying circulation in detail we therefore turn to the study of analogous numerical lenses, similarly arrested through baroclinic instability but within the rather more convenient diagnostic context of a numerical model.

## b. Numerical realizations


### 1) NUMERICAL SET UP


The numerical model employed (described in [Marshall et al. 1997a,b](#)) solves the Boussinesq form of the incompressible Navier–Stokes equations in a rotating frame. The domain of integration, modeled after the geometry of the laboratory tank, takes the form of a cylindrical subdomain of radius 0.58 m and depth 0.15 m inscribed within a Cartesian cube. To accomplish the number of experiments desired, the horizontal and vertical resolution was maximized to 0.01 and 0.005 m respectively yielding  $116 \times 116 \times 30$  elements. The timestep was 0.05 s.





Even for flows confined to a 1-m diameter tank and having scales on the order of only a few centimeters, diffusion of momentum and temperature is necessary to represent unresolved scales and to ensure numerical stability on the numerical grid besides representing *molecular* viscosity and diffusion. At this resolution, isotropic Laplacian mixing was used with momentum and temperature diffusion of, respectively,  $\nu = 5 \times 10^{-6} \text{ m}^2 \text{ s}^{-1}$  and  $K = 1 \times 10^{-7} \text{ m}^2 \text{ s}^{-1}$ . Thus the numerical experiments have a Prandtl number of 50, compared with the laboratory value of 7. Our thermal diffusivity has the same value as that of water but our eddy viscosity  $\nu$  has a value 5 times greater. However, it is important to realize that advection dominates over diffusion in both the laboratory and our numerical experiments, both vertically and horizontally (see, e.g., [Fig. 10](#) ). Thus advection, and not diffusion, is the means by which the warm fluid is pumped down and carried away laterally.



The model was initialized from rest with water of uniform temperature. The simplest equation of state [ $\rho = \rho_o(1 - \alpha T)$ ] was employed such that buoyancy relates to temperature according to the relation  $b = g\alpha T$  where  $\alpha$  is the coefficient of thermal expansion of water. Momentum forcing was achieved by relaxing surface velocities to those over a disc having a differential rotation  $\Delta f$ . Once spun up, the magnitude and spatial homogeneity of the ambient pumping field could be diagnosed from continuity. With establishment of a steady, mechanically driven circulation, a buoyancy source was introduced in the surface layer of the model of magnitude  $B_o$  within a radius  $r_h$  of the center.


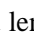
### 2) EVOLUTION OF THE NUMERICAL LENS


With the onset of buoyancy forcing, development and evolution of the resulting warm water lens could be observed and analyzed. The parameters of the 24 numerical experiments analyzed here are given in [Table 2](#) .

[Figure 6](#)  charts the time history of our reference numerical experiment with the parameters highlighted in Table A2. Although it shares the same  $f$ ,  $\Delta f$ ,  $r_h$ , and  $q$  ( $B_o$ ) as the laboratory reference, the Ekman layers are crudely resolved in the numerical model:  $w_{\text{num}} \neq w_{\text{lab}}$  at the modest grid resolution being employed,  $w_{\text{num}}$  being some 30% higher than that assumed to be operative in the laboratory experiment according to [Eq. \(1\)](#). Thus the two lenses are not expected to be directly comparable. The characteristics of the structure and evolution of the numerical lens, however, are very similar to that of the laboratory experiments described previously. Indeed numerical and laboratory results will be combined to test out our theory.




As in the laboratory, there is an initial period of linear growth ([Fig. 6a](#) ) , during which time an increasingly deep, stratified lens of warm water grows down from the surface. Onset of instability is marked by the sudden appearance of a high mode number periodic disturbance on the lens edge ([Fig. 6b](#) ). These small amplitude perturbations grow and, often, coalesce producing waves of large amplitude and wavelength ([Fig. 6c](#) ). An instantaneous picture of the mature, equilibrated, unstable lens system is characterized by an apparently highly disorganized system of irregular eddies ([Fig. 6d](#) ).

[Figure 7](#)  shows the evolution of the central temperature anomaly as a function of time from the numerical reference and may be compared with [Fig. 4](#) . While the overall buoyancy anomaly and depth of the equilibrated lens are not identical in the laboratory and numerical reference, the successive phases of the developing lens are in common. The initial linear phase is succeeded, with the onset of instability, by a slackening in the rate at which the central temperature anomaly accumulates. This is a result of the growing efficiency of the eddies at fluxing buoyancy away from beneath the warming disc. The onset of equilibrium is marked by a flattening of the curve as the lens adopts a constant temperature structure.


[Figure 8a](#)  shows the time-mean equilibrated temperature structure diagnosed from the reference numerical experiment and closely resembles the idealized lens schematized in [Fig. 1](#) ; while instantaneous pictures show little apparent order, a lens of warm, stratified water is clearly revealed in the time mean. The mean flow (as illustrated by the streamlines) carries

high buoyancy water (relative to the mean buoyancy of the entire tank) inward at the surface and then downward to depth. Analysis of the vertical structure, both at the center but now also off-axis ([Fig. 8b](#) ) , demonstrates the same exponential temperature structure seen in the laboratory soundings.


A key strength of the numerical realizations over their laboratory counterparts is the opportunity they provide to diagnose just what terms are important in the flux balance on which the observed quasi-steady lens is contingent.

[Figure 9](#)  defines two control volumes over which we diagnose buoyancy budgets at equilibrium. [Figure 10a](#)  compares the buoyancy fluxes into and out of the first control volume, a cylinder of radius  $r_h$  and depth of the tank. It shows that the input of buoyancy due to heating and convergence of lateral Ekman heat flux at the surface is balanced by lateral eddy buoyancy fluxes over the column. [Figure 10b](#)  compares the buoyancy fluxes into and out of a second, lower control volume—from depth  $h_e$ , the  $e$ -folding depth of the lens, to the bottom of the tank. We see that both vertical and horizontal eddy fluxes balance the input of buoyancy due to Ekman pumping and vertical diffusion. Once again we have a closed balance. Note the negligible contribution diffusion makes to the balance and that eddies, unlike diffusion, transport buoyancy upward.

### 3. Theoretical interpretation

The two key characteristics of our lens are the magnitude of its buoyancy anomaly and the depth scale over which it decays. To determine their dependence on external parameters we will exploit the two buoyancy budgets shown in [Fig. 10](#) .

#### a. Lens parameters

Recalling [Figs. 5 and 8b](#) , let us suppose that the buoyancy anomaly decays from its surface value  $\Delta b_o$ , as  $z \rightarrow -\infty$ , with an  $e$ -folding scale  $h_e$ , thus



$$\Delta b = \Delta b_o(r)e^{z/h_e}. \quad (2)$$

The buoyancy anomaly at the surface, averaged over the heating disc, is then

$$\Delta b_{\text{lens}} = \frac{1}{A} \int_{\text{lens}} \Delta b_o \, dA, \quad (3)$$

where  $A = \pi r_h^2$  is the area of the heating disc. Hereafter the subscript “lens” indicates the surface average. Our goal is to determine the “lens” parameters  $h_e$  and  $\Delta b_{\text{lens}}$  in terms of the “external” parameters  $f$ ,  $r_h$ ,  $w_E$ , and  $B_o$ .

#### b. Buoyancy budgets

To determine our desired expressions for the two parameters  $h_e$  and  $\Delta b_{\text{lens}}$ , we make use of integral buoyancy balances over the two control volumes sketched in [Fig. 9](#) : the first, from  $z = -\infty \rightarrow 0$  and the second from  $z = -\infty \rightarrow -h_e$ . These balances will involve eddy buoyancy fluxes across the boundaries of the control volumes; see [Figs. 9 and 10](#) —which, for us to proceed, must be expressed in terms of mean properties of the lens.

We write the lateral buoyancy flux, thus

$$\overline{v'b'} = -K \frac{\Delta b_{\text{lens}}}{r_h},$$

assuming that the horizontal stratification of the lens,  $\Delta b_{\text{lens}}$ , is uniformly distributed across the heating disc of radius  $r_h$ . Here  $K$  is an eddy transfer coefficient given by

$$K = \overline{v'l'} = c_e u r_h$$

where  $u$  is the mean azimuthal current and  $c_e$  is a constant to be determined experimentally. In the above we have assumed that the eddy transfer scale is set by  $r_h$ , the scale of the baroclinic zone (Green 1970), and that the eddy velocity scale  $\mathbf{v}' \sim u$  (appropriate if the eddies garner energy over a deformation scale; see, e.g., the discussion in section 5 of [Held 1999](#)). Then the above may be combined thus:

$$\overline{\mathbf{v}'b'} = c_e u \Delta b_{\text{lens}}, \quad (4)$$

which is of the form used in [Jones and Marshall \(1997\)](#) in their study of restratification after deep ocean convection.

The thermal wind equation is


$$\frac{\partial u}{\partial z} = \frac{1}{f} \frac{\partial \Delta b}{\partial r} = \frac{1}{f} \frac{\Delta b_{\text{lens}}}{r_h} e^{z/h_e}, \quad (5)$$

where (2) has been used. Integrating (5), assuming that  $u$  decays to zero with depth, yields

$$u = \frac{h_e}{f} \frac{\Delta b_{\text{lens}}}{r_h} e^{z/h_e}. \quad (6)$$

Hence (4) becomes


$$\overline{\mathbf{v}'b'} = c_e \frac{h_e}{f} \frac{\Delta b_{\text{lens}}^2}{r_h} e^{z/h_e}. \quad (7)$$

In the steady state, as we saw in [Fig. 10a](#) , the input of buoyancy at the surface is balanced by lateral eddy buoyancy flux. The surface buoyancy input consists of two parts, the (imposed) surface buoyancy flux,  $B_o$  and the local convergence of buoyancy due the surface Ekman transport,  $\mathbf{v}_E$ . Accordingly, we define an “effective” surface buoyancy flux,  $B^*$ , the net buoyancy delivered to a given point in the surface layer

$$B^* = B_o - \nabla \cdot (\mathbf{v}_E \Delta b_o). \quad (8)$$

Averaging over the heating disc gives a surface influx of buoyancy

$$B_{\text{lens}}^* = B_o + w_E \Delta b_o(r_h), \quad (9)$$

where  $\Delta b_o(r_h)$  is the buoyancy anomaly at the edge of the heating disc. Note that here  $w_E$  is the magnitude of the Ekman pumping; the second term in (9) adds to  $B_o$  so that  $B_{\text{lens}}^* > B_o$  (see [Fig. 10a](#) ). Balancing  $B_{\text{lens}}^*$  with the integrated eddy flux through the side of the lens gives

$$B_{\text{lens}}^* = \frac{2}{r_h} \int_{-\infty}^0 \overline{\mathbf{v}'b'} dz.$$

On substituting for the eddy heat flux using (7), we find that

$$h_e = \left( \frac{1}{2c_e} \right)^{1/2} (f B_{\text{lens}}^*)^{1/2} \frac{r_h}{\Delta b_{\text{lens}}}. \quad (10)$$

The total buoyancy anomaly of the lens is given by

$$= \left( \frac{1}{2c_e} \right)^{1/2} (fB_{\text{lens}}^*)^{1/2} r_h. \quad (11)$$

We now consider the buoyancy balance in the lower portion of the lens, between  $-\infty$  and  $-h_e$ , as diagnosed from the model in [Fig. 10b](#). We obtain

$$w_E \Delta b_{\text{lens}} e^{-1} = \overline{w'b'}^{\text{lens}} + \frac{2}{r_h} \int_{-\infty}^{-h_e} \overline{v'b'} dz, \quad (12)$$

where the vertical advective flux now balances both vertical and lateral eddy fluxes (we have ignored diffusive fluxes which are an order of magnitude smaller than advective ones (see [Fig. 10b](#))).

Now, if the ratio of vertical eddy buoyancy flux to horizontal eddy flux is roughly the mean isopycnal slope, we can write

$$\overline{w'b'}^{\text{lens}} = \frac{\alpha}{h_e} \int_{-\infty}^{-h_e} \overline{v'b'} dz, \quad (13)$$

where

$$\alpha = \alpha' \frac{h_e}{r_h} \quad (14)$$

is proportional to the isopycnal slope as measured by  $h_e/r_h$  with  $\alpha' \approx 1$ . From [Fig. 10b](#), we see that for our reference numerical experiment the vertical eddy flux—the first term on the right-hand side of (12)—is roughly 2/3 of the horizontal eddy flux, the second term on the right hand side of (12). From (13) and (14), we thus deduce that  $\alpha'$  is indeed close to unity for this experiment.

The integral balance (12) then yields, using (7):

$$h_e^2 = \frac{1}{c_e(2 + \alpha')} \frac{w_E}{\Delta b_{\text{lens}}} f r_h^2. \quad (15)$$

### c. Prediction for depth and buoyancy anomaly of lens

Dividing (15) by (10) we obtain

$$h_e = c_{h_e} \left( \frac{f}{B_{\text{lens}}^*} \right)^{1/2} w_E r_h, \quad (16)$$

where

$$c_{h_e} = \left( \frac{2}{c_e} \right)^{1/2} \frac{1}{(2 + \alpha')}. \quad (17)$$

Combining (16) and (10) we find that

$$\Delta b_{\text{lens}} = c_{\Delta b} \frac{B_{\text{lens}}^*}{w_E}, \quad (18)$$

where

$$c_{\Delta b} = \frac{2 + \alpha'}{2}. \quad (19)$$

[Equations \(16\) and \(18\)](#) are our predictions for the depth and buoyancy anomaly of the lens.

#### d. Testing theory against experiment

Combining the results from the laboratory and numerical experiments tabulated in Tables A1 and A2, lens parameters—temperatures and depths—were analyzed and, as we now describe, rationalized in terms of the theory just presented.

In order to test our theoretical predictions against our numerical and laboratory experiments we first examined the time and axially averaged buoyancy values of the lens obtained in the numerical experiments set out in Table A2. The total buoyancy anomaly was found by integrating over the radius of the heating disc and over depth and dividing by the area of the heating disc.

In [Fig. 11](#) we plot the calculated total buoyancy versus the formula in [\(11\)](#). Taking the best fit line through the points gives that

$$h_e \Delta b_{\text{lens}} = 2.03 (B_{\text{lens}}^* f)^{1/2} r_h, \quad (20)$$

in support of [\(11\)](#). [Equation \(10\)](#) then implies that  $c_e = 0.12$ . This value is of the same order, but somewhat larger than the 0.04 obtained by [Jones and Marshall \(1997\)](#) in their study of lateral heat exchange in the baroclinic instability of mixed layers formed in deep convection.

[Equation \(20\)](#) is interesting because it tells us that the deformation radius  $L_\rho$  is given by

$$L_\rho^2 = \frac{h_e \Delta b_{\text{lens}}}{f^2} = 2.03 \left( \frac{B^*}{f^3} \right)^{1/2} r_h.$$

Thus

$$L_\rho \approx (L_{\text{rot}} r_h)^{1/2}$$

where  $L_{\text{rot}} = (B^*/f^3)^{1/2}$  is the length scale that controls rotating convection; see [Jones and Marshall \(1993\)](#) and [Marshall and Schott \(1999\)](#). In our experiments,  $L_{\text{rot}} \approx 10^{-3}$  m compared to  $r_h \approx 10^{-1}$  m. Thus  $L_{\text{rot}}/r_h \ll 1$  and our equilibrated lens is far from the baroclinically neutral state of  $L_{\text{rot}}/r_h \approx 1$ .

In [Fig. 12](#) we plot  $\Delta b_{\text{lens}}$  versus the prediction [\(18\)](#). Taking the best fit line to the points, gives

$$\Delta b_{\text{lens}} = 1.38 \left( \frac{B_{\text{lens}}^*}{W_E} \right), \quad (21)$$

which, from [Eq. \(19\)](#), implies that  $\alpha' = 0.76$ . Note that in [Fig. 12](#) both numerical and laboratory points are plotted. To compute values of  $B_{\text{lens}}^*$  for the laboratory, [Eq. \(9\)](#), the total buoyancy supplied to the surface layer by both surface heating and Ekman processes is required. In the absence of direct axial measurements in the laboratory experiments, we assume the radial structure of the laboratory lenses has the same form as that of their numerical counterparts.

[Figure 13](#) shows that for the numerical lenses the buoyancy at the edge of the heating disc,  $\Delta b_o(r_h)$ , is simply a constant fraction of the average lens anomaly  $\Delta b_{\text{lens}}$ . The points cluster along a straight line yielding

$$\Delta b_o(r_h) = 0.72 \Delta b_{\text{lens}}, \quad (22)$$



the relation used to plot the laboratory points in [Fig. 12](#).

To quantify the depth of the lens, we radially average the buoyancy anomaly and fit an exponential curve to the resulting vertical profile. In [Fig. 14](#) we plot the  $e$ -folding depth of the lens versus the formula [\(16\)](#). The line plotted through the points, gives

$$h_e = 0.93 \left( \frac{f}{B_{\text{lens}}^*} \right)^{1/2} w_E r_h. \quad (23)$$

Using [\(22\)](#) and [\(21\)](#) we find that [\(9\)](#) can be written

$$B_{\text{lens}}^* = 5.8 B_{\text{lens}}. \quad (24)$$

This indicates that, when the lens has reached a steady state, the buoyancy supplied to the surface is largely determined by the Ekman convergence of buoyancy rather than the surface heating. Thus, at steady state, the leading order horizontal balance is between the Ekman convergence of buoyancy and the outward eddy transport of buoyancy. This does not imply, of course, that the heating does not play an essential role in the creation of the lens!

#### 4. Conclusions

We have set up laboratory and numerical experiments in which we pump warm water down from the surface of an initially homogeneous rotating fluid. The heating creates a temperature gradient while pumping advects the isotherms downward, creating a deepening warm water lens surrounded by colder ambient fluid. Currents develop in thermal wind balance with the lateral temperature gradients. They become baroclinically unstable and the resulting swirls and meanders carry warmed stratified fluid away to the periphery and bring cooler ambient fluid inward under the heating. The effect of this exchange is to arrest the deepening and warming of the lens. The equilibrium state is one in which the lateral transfer of heat by geostrophic eddies exactly balances the temperature gain at the surface—potential energy created by the collusion of mechanical and buoyancy forcing is exactly balanced by its destruction through baroclinic instability, just as hypothesized by [Gill et al. \(1974\)](#). The experiments were specifically tailored to focus on this process in isolation, to unambiguously evaluate the potential for eddies to balance surface forcing and establish a stratification.

There are several important conclusions that follow from our experiments and theory. First, the spacing between the isentropes, seen for example in [Figs. 4 or 6](#), is controlled by baroclinic instability rather than small-scale mixing. Baroclinic eddies sweep fluid laterally away from under the heating source to the periphery where, by other physical processes, the warm fluid cools. Second, the eddy flux, to leading order, balances the wind driven overturning circulation (the Ekman transport and pumping) as can be clearly seen in [Fig. 10](#). In so doing, advection of buoyancy induced by eddies largely cancels that due to the wind-driven flow. The net advection—the residual circulation—carries heat away from the lens to balance the heating. These balances can be elegantly expressed in terms of “residual mean theory,” as discussed in the companion paper—see [Karsten et al. \(2001\)](#).

The simple ideas explored here broadly account for the laboratory and numerical experiments described. The buoyancy anomaly and depth of penetration of the warm, pumped lenses were successfully rationalized in terms of theory, at the heart of which is the eddy closure [Eq. \(4\)](#). But could the ideas presented here have any relevance for the large-scale ocean circulation? Let us provisionally suppose that the formulas [\[Eqs. \(21\) and \(23\)\]](#) are relevant to the ocean. What do they predict about the depth and stratification of the main thermocline?

First, we must consider the buoyancy forcing  $B^*$ . Much of the buoyancy supplied to subtropical ocean gyres emanates from the tropics rather than by warming/freshening through in situ air–sea interaction. In the North Atlantic, for example, heat is advected northwards in the Ekman layers associated with the trade winds. This can be readily seen in the diagnostic study of [Marshall et al. \(1993\)](#); see [Fig. 13](#) where an  $H_{\text{pump}}$  (the heat supplied through Ekman processes, equivalent in this study to the second term on the right-hand side of [Eq. \(8\)](#)), reaches  $20 \text{ W m}^{-2}$ , with a mean over the gyre of perhaps  $10 \text{ W m}^{-2}$ . Locally, the buoyancy flux through the sea surface is much smaller and, if anything, negative over the subtropics. Thus, in nature, as observed in our experiments here, there is a distinction between  $B$  and  $B^*$ . The wind acts not only to pump fluid down from the surface, but also, through horizontal advection from the south, to bring in significant warmth to maintain the buoyancy of the subtropical gyre.

Typical values of  $w_E$  and  $r_h$  are readily estimated from the scale and amplitude of the prevailing wind patterns. Setting  $w_E = 50 \text{ m yr}^{-1}$ ,  $r_h = 2 \times 10^6 \text{ m}$ ,  $f = 10^{-4} \text{ s}^{-1}$ , and assuming  $10 \text{ W m}^{-2}$  mean heat flux supplied to the Ekman layer, yielding a

$B^* \sim 5 \times 10^{-9} \text{ m}^2 \text{ s}^{-3}$ , we find, using [Eqs. \(23\) and \(21\)](#), that  $h_e \sim 450 \text{ m}$  and  $\Delta T \sim 8 \text{ K}$ . These are interesting numbers.

That they are a significant fraction of the corresponding scales typically observed in a subtropical ocean gyre suggests that our basic thesis—that eddies could be a fundamental player in setting ocean stratification—may have some merit.

However, the simplicity of the problem constructed here—excluding Sverdrup dynamics,  $\beta$  effect, or western boundary currents—makes it too simple for the results to be applied so directly to the ocean. In ocean gyres integral balances are likely to be disjoint, with intense jets, such as the separated Gulf Stream, making large local contributions. Further studies, to be reported later, will incorporate Sverdrup dynamics and western boundary currents in the context of gyre-scale circulations. This should enable us to evaluate the mechanism we are focusing on here in a more complex and realistic setting.

Before concluding, it should be mentioned that eddies are not often ascribed a central role in ocean circulation theory, except perhaps to “mop up” some untidiness in the western margin of the basin. There is a body of thermocline theory beginning with Robinson and Stommel (1958) that invokes diapycnal mixing to set the vertical stratification. Recently [Salmon \(1990\)](#) associates the thermocline with an internal front maintained diffusively. [Niiler \(1966\)](#) invoked eddy processes to constrain near-inertial theories of the barotropic ocean circulation. Modern thermocline theory, starting from seminal papers of [Rhines and Young \(1982\)](#), invoked geostrophic eddies to “homogenize” quasi-geostrophic potential vorticity, so setting the perturbation about a prescribed reference stratification. But since then—partly because of the success of laminar “ventilated thermocline theory” of [Luyten et al. \(1983\)](#)—there has been a retreat from ascribing eddies a central role in setting the structure of the thermocline. Reviews of the appropriate literature can be found in [Rhines \(1986\)](#) and [Pedlosky \(1996\)](#). An attempt to combine ventilated and diffusive thermocline theory together is provided by [Samelson and Vallis \(1997\)](#) and [Vallis \(2000\)](#).

Our thesis here is that the heat pumped down from the Ekman layers is not diffused away vertically; rather the balancing mechanism is lateral transfer of heat by eddies. Observations show us that the ocean is teeming with eddies. Indeed, over much of the ocean's interior the energy contained in the eddy field far exceeds that contained in the mean (see, e.g., the observations presented in [Stammer 1998](#)). Process studies such as [Spall \(2000\)](#) suggest significant eddy energy anywhere there is meridional flow. As resolution increases, more realistic models have also begun to capture this energetic eddy field: see, for example, the early study of [Cox \(1985\)](#). In numerical models of ocean circulation eddies do transport a significant amount of heat, but it is difficult to assess their contribution in isolation because a “compensation” is observed: eddy fluxes of heat being balanced by the eddy-induced change in mean flow heat advection ([Böning and Budich 1992](#)). Moreover, due to their computational expense, such calculations can be carried out only for several decades and remain far from the equilibrium state that is the focus of attention here.

Perhaps, as they stand, our ideas are most relevant to the Antarctic Circumpolar Current (ACC) where Sverdrup dynamics is less of a constraint and zonal-average theory is most relevant. In the Southern Ocean there is a surface temperature gradient induced by cooling around Antarctica and warming in the subtropics. In addition, the predominantly zonal winds drive a meridional circulation—the Deacon Cell—that acts to overturn the isopycnals. Pumping of warm fluid down in the subtropics is analogous to the problem discussed here, while the cooling and upwelling south of the current enhance the established front. Baroclinic instability of the associated thermal wind extracts potential energy and tends to flatten the isopycnals. [Gnanadesikan \(1999\)](#) and [Vallis \(2000\)](#) have noted the possible importance of the Southern Ocean in setting thermocline structure. Their models emphasize mixing across the ACC, a region of high eddy activity. Based on the analysis presented here we expect baroclinic eddies, in collusion with forcing from winds and air–sea fluxes, to set the stratification and transport of the ACC. The dynamics of the ACC is explored from this perspective in a companion paper—[Karsten et al. \(2001\)](#).

### Acknowledgments

We thank the Physical Oceanography Division of the National Science Foundation whose support made this study possible. The laboratory experiments could not have been carried out without the expert advice and encouragement of Jack Whitehead at Woods Hole. R.H.K. was supported in part by an NSERC PDF.

---

## REFERENCES

- Böning C. W., and R. C. Budich, 1992: Eddy dynamics in a primitive equation model: sensitivity to horizontal resolution and friction. *J. Phys. Oceanogr.*, **22**, 361–381. [Find this article online](#)
- Cox M. D., 1985: An eddy resolving numerical model of the ventilated thermocline, time dependence. *J. Phys. Oceanogr.*, **15**, 1312–1324. [Find this article online](#)
- Gill A. E., J. S. A. Green, and A. J. Simmons, 1974: Energy partition in the large-scale ocean circulation and the production of mid-ocean

eddies. *Deep-Sea Res*, **21**, 499–528. [Find this article online](#)

Gnanadesikan A., 1999: A simple predictive model for the structure of the oceanic pycnocline. *Science*, **283**, 2077–2079. [Find this article online](#)

Green J. S. A., 1970: Transfer properties of the large scale eddies and the general circulation of the atmosphere. *Quart. J. Roy. Meteor. Soc*, **96**, 157–185. [Find this article online](#)

Held I., 1999: The macroturbulence of the troposphere. *Tellus*, **51A–B**, 59–70. [Find this article online](#)

Hide R., and C. W. Titman, 1967: Detached shear layers in a rotating fluid. *J. Fluid. Mech*, **29**(1), 39–60. [Find this article online](#)

Jones H., and J. Marshall, 1993: Convection with rotation in a neutral ocean: A study of open-ocean deep convection. *J. Phys. Oceanogr*, **23**, 1009–1039. [Find this article online](#)

Jones H., and J. Marshall, 1997: Restratification after deep convection. *J. Phys. Oceanogr*, **27**, 2276–2287. [Find this article online](#)

Karsten R., H. Jones, and J. Marshall, 2002: The role of eddy transfer in setting the stratification and transport of a Circumpolar Current. *J. Phys. Oceanogr*, **32**, 39–54. [Find this article online](#)

Luyten J., J. Pedlosky, and H. Stommel, 1983: The ventilated thermocline. *J. Phys. Oceanogr*, **13**, 292–309. [Find this article online](#)

Marshall J., and F. Schott, 1999: Open ocean deep convection: Observations, models and theory. *Rev. Geophys*, **37**, 1–64. [Find this article online](#)

Marshall J., A. J. G. Nurser, and R. Williams, 1993: Inferring the subduction rate and period over the North Atlantic. *J. Phys. Oceanogr*, **23**, 1315–1329. [Find this article online](#)

Marshall J., A. Adcroft, C. Hill, L. Perelman, and C. Heisey, 1997a: A finite-volume, incompressible Navier Stokes model for studies of the ocean on parallel computers. *J. Geophys. Res*, **102**, 5753–5766, (C3). [Find this article online](#)

Marshall J., C. Hill, L. Perelman, and A. Adcroft, 1997b: Hydrostatic, quasi-hydrostatic, and nonhydrostatic ocean modeling. *J. Geophys. Res*, **55**, 201–222. [Find this article online](#)

Niiler P., 1966: On the theory of the wind-driven ocean circulation. *Deep-Sea Res*, **13**, 597–606. [Find this article online](#)

Pedlosky J., 1987: *Geophysical Fluid Dynamics*. 2d ed. Springer-Verlag, 710 pp.

Pedlosky J., 1996: *Ocean Circulation Theory*. Springer-Verlag, 420 pp.

Rhines P. B., 1986: Vorticity dynamics of the oceanic general circulation. *Ann. Rev. Fluid Mech*, **18**, 433–497. [Find this article online](#)

Rhines P. B., and W. R. Young, 1982: A theory of the wind-driven circulation I: Mid-ocean gyres. *J. Mar. Res*, **40**, 559–596, (Suppl.). [Find this article online](#)

Robinson A. R., and H. Stommel, 1959: The oceanic thermocline and the associated thermohaline circulation. *Tellus*, **11**, 259–308. [Find this article online](#)

Salmon R., 1990: The thermocline as an “internal boundary layer.”. *J. Mar. Res*, **48**, 437–469. [Find this article online](#)

Samelson R. M., and G. K. Vallis, 1997: Large-scale circulation with small diapycnal diffusion: The two-thermocline limit. *J. Mar. Res*, **55**, 223–275. [Find this article online](#)

Spall M. A., 2000: Generation of strong mesoscale eddies by weak ocean gyres. *J. Mar. Res*, **58**, 97–116. [Find this article online](#)

Stammer D., 1998: On eddy characteristics, eddy transports, and mean flow properties. *J. Phys. Oceanogr*, **28**, 727–739. [Find this article online](#)

Stone P. H., 1972: A simplified radiative-dynamical model for the static stability of rotating atmospheres. *J. Atmos. Sci*, **29**, 405–418. [Find this article online](#)

Vallis G. K., 2000: Large-scale circulation and production of stratification: Effects of wind, geometry and diffusion. *J. Phys. Oceanogr*, **30**, 933–954. [Find this article online](#)

---

## Tables

TABLE 1. Parameter values for the laboratory experiments. The values for the reference experiment discussed in detail are highlighted in bold

$f$ (s <sup>-1</sup> )	$r_s$ (m)	$B_0$ $\times 10^{-6}$ (m <sup>2</sup> s <sup>-3</sup> )	$-w_E$ $\times 10^{-3}$ (m s <sup>-1</sup> )	$h_0$ $\times 10^{-2}$ (m)	$\Delta b$ $\times 10^{-2}$ (m s <sup>-2</sup> )
0.54	0.15	0.38	0.04	0.71	1.83
0.54	0.15	1.41	0.20	0.63	4.65
<b>0.75</b>	<b>0.15</b>	<b>0.25</b>	<b>0.06</b>	<b>0.77</b>	<b>1.55</b>
0.75	0.15	1.01	0.40	1.71	1.30
1.00	0.15	0.09	0.05	1.44	0.62
1.50	0.15	0.33	0.05	1.04	2.36
1.75	0.15	0.06	0.03	1.55	0.41
2.75	0.15	0.47	0.21	2.83	1.09
2.75	0.15	0.48	0.21	3.68	1.04
2.75	0.15	0.48	0.21	2.96	1.25

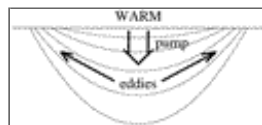
[Click on thumbnail for full-sized image.](#)

TABLE 2. Parameter values for the numerical experiments. The values for the reference experiment discussed in detail are highlighted in bold

$f$ (s <sup>-1</sup> )	$r_s$ (m)	$B_0$ $\times 10^{-6}$ (m <sup>2</sup> s <sup>-3</sup> )	$-w_E$ $\times 10^{-3}$ (m s <sup>-1</sup> )	$h_0$ $\times 10^{-2}$ (m)	$\Delta b$ $\times 10^{-2}$ (m s <sup>-2</sup> )
0.75	0.10	0.25	0.08	1.22	2.11
0.50	0.15	0.07	0.10	1.53	0.98
0.50	0.15	0.12	0.21	1.32	1.32
0.75	0.15	0.06	0.08	1.69	0.87
0.75	0.15	0.12	0.08	1.53	1.61
<b>0.75</b>	<b>0.15</b>	<b>0.25</b>	<b>0.08</b>	<b>1.42</b>	<b>2.83</b>
0.75	0.15	0.25	0.08	1.39	2.42
0.75	0.15	0.25	0.11	1.51	2.55
0.75	0.15	0.12	0.12	1.80	1.27
0.75	0.15	0.25	0.15	1.42	2.70
0.75	0.15	0.25	0.11	1.34	2.50
0.75	0.15	0.12	0.18	1.35	1.12
0.75	0.15	0.12	0.26	1.84	1.34
1.00	0.15	0.58	0.07	1.16	5.56
1.00	0.15	0.02	0.09	3.17	0.30
1.00	0.15	0.12	0.17	1.72	1.46
1.75	0.15	0.06	0.06	2.55	0.59
1.75	0.15	0.25	0.06	1.52	3.06
0.75	0.20	0.25	0.08	1.71	1.44
0.75	0.25	0.12	0.08	2.20	2.20
0.75	0.25	0.25	0.08	1.68	3.42
0.75	0.15	0.25	0.08	1.47	3.44
0.75	0.15	0.25	0.04	1.16	2.64
0.75	0.15	0.17	0.06	1.32	2.25

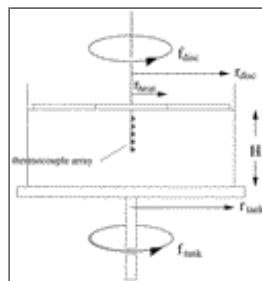
[Click on thumbnail for full-sized image.](#)

## Figures



[Click on thumbnail for full-sized image.](#)

FIG. 1. Schematic representation of a lens of warm water created at the surface by heating and pumped down by the mechanical action of the wind. The deepening of the lens is arrested by its baroclinic instability



[Click on thumbnail for full-sized image.](#)

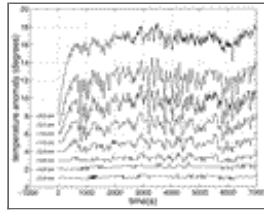
FIG. 2. Side-view schematic of the experimental apparatus. The working fluid is contained in a cylindrical region of diameter 115 cm and depth 15 cm. At the upper surface, the fluid is forced mechanically to a radius of 55 cm and heated over a circular region of radius 15 cm





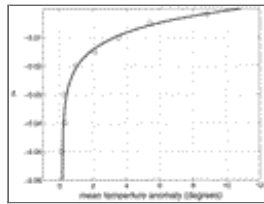
[Click on thumbnail for full-sized image.](#)

FIG. 3. A photograph from the reference laboratory experiment. Dye streaks injected at the edge of the heating pad demonstrate the presence of baroclinic eddies



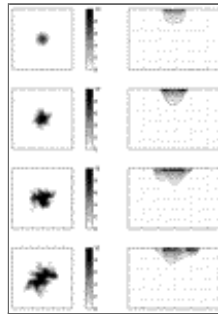
[Click on thumbnail for full-sized image.](#)

FIG. 4. Temperature against time traces recorded by the eight axial thermocouples from the reference laboratory experiment



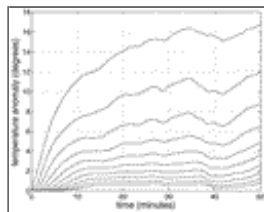
[Click on thumbnail for full-sized image.](#)

FIG. 5. Time-mean profile for the reference laboratory lens. The circles mark the actual mean temperatures measured at each thermocouple with the curve indicating the best fit exponential



[Click on thumbnail for full-sized image.](#)

FIG. 6. Evolution of the reference numerical lens. On the left is the developing surface temperature field (at a depth of 0.75 cm) after 10, 18, 30, and 45 minutes of heating. On the right are corresponding mid-domain, vertical temperature sections. The ambient temperature is 20°C. The contour interval is 1°C



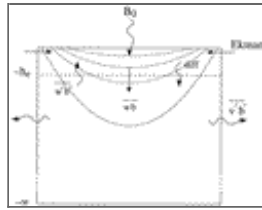
[Click on thumbnail for full-sized image.](#)

FIG. 7. Temperature against time traces for the 10 nearest surface levels diagnosed from the reference numerical experiment



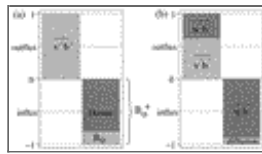
[Click on thumbnail for full-sized image.](#)

FIG. 8. (a) The radially averaged time-mean temperature profile of the equilibrated reference numerical lens (full) with accompanying mean flow streamlines (dashed). (b) All 15 vertical profiles (normalized by their surface value) for the temperature beneath the heating at steady state



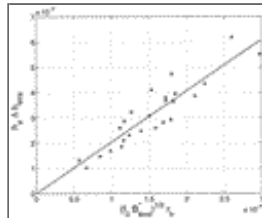
[Click on thumbnail for full-sized image.](#)

FIG. 9. To analyze eddy and diffusive fluxes we define a control volume of radius  $r_h$  and the full depth of the tank  $H$ . This cylinder is then divided into two regions: a surface subvolume of depth  $h_e$ , the  $e$ -folding scale of the buoyancy anomaly, and the remainder beneath



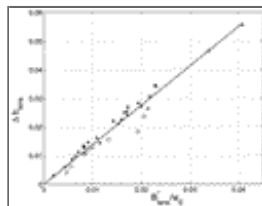
[Click on thumbnail for full-sized image.](#)

FIG. 10. (a) A histogram of the (normalized) buoyancy flux balance into and out of the volume extending over the entire depth of the tank,  $z = -\infty \rightarrow 0$ . Clearly demonstrated is the close balance between  $B_o^*$ , the effective surface flux (a combination of the imposed surface flux  $B_o$  and Ekman convergence) and the total flux out of the volume due to the eddies. (b) A histogram of the (normalized) buoyancy flux balance into and out of the volume below a depth  $h_e$ ,  $z = -\infty \rightarrow -h_e$ . To the left are the horizontal and vertical components of the outflux (due to the eddies) and their sum; to the right the contributions of Ekman pumping and diffusion to the influx through the top surface and their sum. Evident is the significant vertical eddy transport component as well as the negligible role of diffusion in the balance



[Click on thumbnail for full-sized image.](#)

FIG. 11. Plot of the total buoyancy  $h_e \Delta b_{\text{lens}}$  vs  $(fB_o^*)^{1/2} r_h$



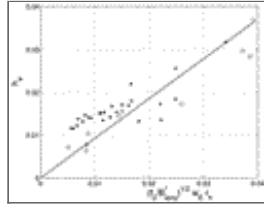
[Click on thumbnail for full-sized image.](#)

FIG. 12. Plot of  $\Delta b_{\text{lens}}$  vs  $B_o^*/w_E$  for the laboratory (circles) and numerical (stars) experiments



Click on thumbnail for full-sized image.

FIG. 13. Plot of  $\Delta b_o(r_h)$  vs  $\Delta b_{\text{lens}}$



Click on thumbnail for full-sized image.

FIG. 14. Plot of  $h_e$ , the  $e$ -folding depth of the lens, vs  $(f/B_{\text{lens}}^*)^{1/2} w_{Eh} r_h$  for the laboratory (circles) and numerical (stars) experiments

Corresponding author address: Dr. John Marshall, Dept. of Earth, Atmospheric and Planetary Sciences, Massachusetts Institute of Technology, 54-1526, Cambridge, MA 02139-4307. E-mail: [marshall@gulf.mit.edu](mailto:marshall@gulf.mit.edu)

top ▲



© 2008 American Meteorological Society [Privacy Policy and Disclaimer](#)  
Headquarters: 45 Beacon Street Boston, MA 02108-3693  
DC Office: 1120 G Street, NW, Suite 800 Washington DC, 20005-3826  
[amsinfo@ametsoc.org](mailto:amsinfo@ametsoc.org) Phone: 617-227-2425 Fax: 617-742-8718  
[Allen Press, Inc.](#) assists in the online publication of AMS journals.